MATERIALS SCIENCE

Etching gas-sieving nanopores in single-layer graphene with an angstrom precision for high-performance gas mixture separation

J. Zhao[1,2]*, G. He[1]*, S. Huang[1], L. F. Villalobos[1], M. Dakhchoune[1], H. Bassas[1], K. V. Agrawal[1]†

Copyright © 2019 The Authors, some rights reserved; exclusive licensee American Association for the Advancement of Science. No claim to original U.S. Government Works. Distributed under a Creative Commons Attribution NonCommercial License 4.0 (CC BY-NC).

One of the bottlenecks in realizing the potential of atom-thick graphene membrane for gas sieving is the difficulty in incorporating nanopores in an otherwise impermeable graphene lattice, with an angstrom precision at a high-enough pore density. We realize this design by developing a synergistic, partially decoupled defect nucleation and pore expansion strategy using O_2 plasma and O_3 treatment. A high density (ca. 2.1×10^{12} cm^{-2}) of H_2-sieving pores was achieved while limiting the percentage of CH_4-permeating pores to 13 to 22 parts per million. As a result, a record-high gas mixture separation performance was achieved (H_2 permeance, 1340 to 6045 gas permeation units; H_2/CH_4 separation factor, 15.6 to 25.1; H_2/C_3H_8 separation factor, 38.0 to 57.8). This highly scalable pore etching strategy will accelerate the development of single-layer graphene-based energy-efficient membranes.

INTRODUCTION

The incorporation of angstrom-sized pores in single-layer graphene at moderate to high density is highly desirable to achieve an ultrahigh separation performance, attributing to the fact that graphene is the thinnest molecular barrier (*1*–*6*). Several molecular simulations and transport calculations have shown that a single-layer graphene, hosting a high density of size-selective pores, can separate molecules by the size-sieving mechanism while yielding several orders of magnitude higher permeance than that from the state-of-the-art polymeric and nanoporous membranes [zeolites, metal-organic frameworks (MOFs), graphene oxide (GO), carbon molecular sieves (CMS), etc.] (*6*–*11*). We recently demonstrated that single-layer graphene, hosting a low density of intrinsic defects (5.4×10^{10} cm^{-2}), can yield an attractive gas separation performance (*5*). To realize the true potential of the single-layer graphene membranes, it is imperative to synthesize nanoporous graphene with a high porosity. The direct bottom-up crystallization of nanoporous graphene by the Ullmann coupling route is highly promising; however, as of now, the lattice disorder in these crystals is too high, and as such, a meaningful molecular separation cannot be achieved (*12*). A practical approach toward the nanoporous single-layer graphene is to incorporate molecular-sized pores in the graphene lattice via a post-synthetic etching (*3*, *13*, *14*). The major bottleneck in this approach is that the available etching chemistries yielding a high-enough pore density (> 10^{12} cm^{-2}) also incorporate a large population of larger nonselective nanopores that dominate the overall gas transport via the effusive transport mechanism (*2*). Therefore, the development of a highly controllable lattice etching technique, working against the trade-off between the pore density and the pore size distribution (PSD), is highly attractive. The state-of-the-art nanofabrication techniques, using focused ion and focused electron beams, are restricted to a resolution of 1 nm (*2*, *15*, *16*). In comparison, the oxidative etching techniques (ultraviolet light, oxygen, oxygen plasma, O_3, etc.) have been shown to generate subnanometer pores (*1*, *4*, *5*, *17*); however, so far, they have not yielded the needed porosity and PSD for the synthesis of high-performance graphene membranes for gas separation (*18*).

The pore generation in the graphene lattice is somewhat analogous to the crystal nucleation and growth; it involves nucleation of defects followed by the pore growth. Here, the nuclei correspond to the vacancy defects or the sp^3 defects, which eventually yield vacancy defects. Generally, the synthesis of monodispersed crystals involves a nucleation burst (*19*). Analogously, nanopores with a narrow PSD can be etched by the generation of a high density of nuclei, followed by a controlled pore expansion. For instance, the oxygen plasma, containing a high concentration of reactive ions and free radicals, can incorporate a high density of nuclei in less than 1 s (*20*). By exposing these nuclei to a well-controlled concentration of oxygen atoms for an optimized time and reaction temperature, one can potentially control the pore expansion rate. Thus, it is envisaged that a high density of molecular-sized pores with a narrow PSD can be etched in graphene if the nucleus formation and the pore expansion are decoupled. Herein, we report a successful implementation of this partially decoupled defect nucleation and pore expansion strategy with O_2 plasma and O_3 (Fig. 1), achieving a high density of H_2-sieving nanopores (up to 2.1×10^{12} cm^{-2}) while limiting the percentage of CH_4 permeating pores to 13 to 22 parts per million (ppm). We apply these nanopores for the gas separation, especially the H_2/CH_4 and H_2/C_3H_8 separations. The purification of hydrogen from light hydrocarbons has extensive applications in the chemical and petrochemical industries. Examples include olefin production by alkane dehydrogenation reaction and hydrogen recovery from the refinery off-gas streams. Keeping this in mind, we investigated H_2/CH_4 and H_2/C_3H_8 separations as a function of the defect nucleation and pore expansion strategy applied in this study. A record-high mixed-gas separation performance was achieved [H_2 permeance, 1340 to 6045 gas permeation units (GPU); H_2/CH_4 separation factor (SF), 15.6 to 25.1; H_2/C_3H_8 SF, 38.0 to 57.8].

RESULTS

Nanoporous single-layer graphene

The single-layer graphene was synthesized on a Cu foil by low-pressure chemical vapor deposition (LPCVD) (*21*). The uniform surface morphology (Fig. 2A) combined with an I_D/I_G ratio of 0.04 ± 0.01 (Fig. 2B) and an I_{2D}/I_G ratio greater than 2 (Fig. 2C) confirmed that the as-synthesized graphene was a single layer and hosted a low density

[1]Laboratory of Advanced Separations (LAS), École Polytechnique Fédérale de Lausanne (EPFL), Sion CH-1951, Switzerland. [2]State Key Laboratory of Materials-Oriented Chemical Engineering, Jiangsu National Synergetic Innovation Center for Advanced Materials, College of Chemical Engineering, Nanjing Tech University, Nanjing 210009, China.
*These authors contributed equally to this work.
†Corresponding author. Email: kumar.agrawal@epfl.ch

Downloaded from http://advances.sciencemag.org/ on January 27, 2019

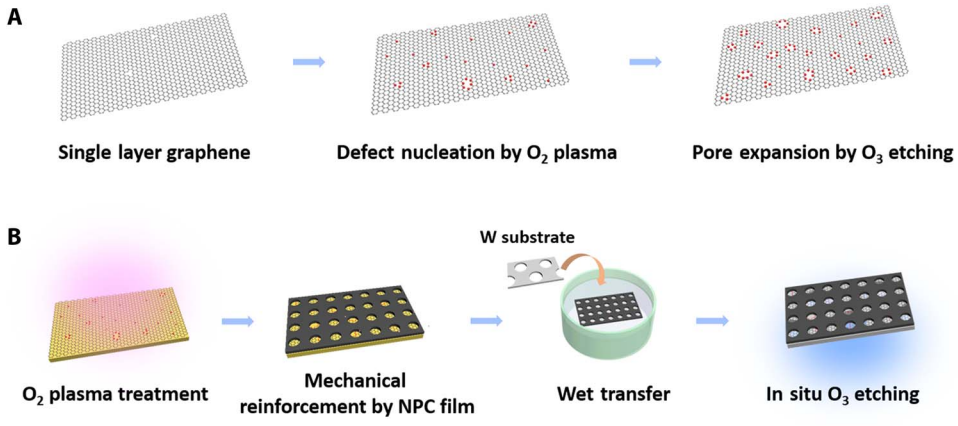

Fig. 1. Schematic of the partially decoupled defect nucleation and pore expansion. (**A**) Evolution of graphene lattice after subsequent exposures to O_2 plasma and O_3. (**B**) Fabrication procedure for nanoporous graphene membrane. The ozone treatment was carried out in situ.

of intrinsic defects (1.5×10^{10} cm^{-2}) (fig. S1) (*22*). After exposing the as-synthesized graphene to the O_2 plasma, the I_D/I_G ratio, indicative of the lattice disorder, increased with the plasma exposure up to 3 s (from 0.04 to 2.08; Fig. 2, D and E), while conversely, the I_{2D}/I_G ratio decreased (Fig. 2E). With a longer exposure time (>3 s), the I_D/I_G ratio decreased with the plasma time. This effect can be explained by the fact that at higher plasma time, the sp^3 defects and porosity are expected to increase, decreasing the number of ordered six-atom rings (Fig. 2E) (*23*). We did not observe pronounced amorphization of the graphene lattice even after 6 s of plasma treatment (fig. S2 and note S1). Besides, after the 2 s of plasma exposure, an obvious D′ peak appeared, and $I_{D'}$ increased further with the plasma time. The $I_D/I_{D'}$ ratio can be used to distinguish predominantly sp^3-type defects ($I_D/I_{D'} > 7$) and predominantly vacancy-type defects ($I_D/I_{D'} < 7$) (*24*). On the basis of the trend of $I_D/I_{D'}$ with plasma time (Fig. 2F), for exposure up to 1 s, the majority of defects appear to be sp^3 type; however, the generation of the vacancy defects cannot be completely ruled out.

After exposing graphene to the O_2 plasma, our recently reported nanoporous carbon (NPC) film–assisted transfer method was applied to fabricate crack- and tear-free graphene membranes on a macroporous W substrate hosting arrays of 5-μm pores over a 1-mm^2 area (schematic in Fig. 1B) (*5*). Briefly, a solution of block copolymer and turanose was spin coated on graphene, forming ordered cylindrical domains due to phase separation during drying. This was followed by pyrolysis at 500°C, which led to the carbonization of the film and yielded an NPC support film comprising 20- to 30-nm-sized pores (Fig. 3A). The NPC film adhered strongly to the graphene film, conferring it the sufficient mechanical support for the application as a suspended membrane. An excellent bonding between the NPC and the graphene film was confirmed by the presence of the typical electron diffraction (ED) pattern of single-layer graphene along the [001] zone axis, which was present throughout the sample (Fig. 3B). For membrane fabrication, the NPC/graphene was transferred onto a macroporous W substrate. The presence of NPC on top of the graphene prevented the formation of crack and tear during the transfer (Fig. 3, C to E). The composite film was uniform and was ca. 80 nm thick (Fig. 3F).

Molecular transport properties of plasma-treated graphene

The molecular transport properties from as-synthesized and plasma-treated graphene were evaluated by the gas permeation experiments to understand the evolution of pore density and PSD. The intrinsic defects in all four as-synthesized graphene membranes (M1 to M4) displayed temperature-activated H_2 transport with an average activation energy of 16.3 ± 0.1 kJ mol^{-1} (note S2), an average permeance of 194 ± 46 GPU, and an average H_2/CH_4 selectivity of 18.6 ± 4.0 at 150°C (Fig. 4 and tables S1 to S3). The C_3H_8 and SF_6 permeances were too low to be detected. On the basis of the detection limit of our mass spectrometer, the H_2/C_3H_8 and the H_2/SF_6 selectivities were greater than 100.

A 1-s plasma treatment significantly improved the hydrogen permeance, following a significant increase in the defect density (3.0×10^{11} cm^{-2}) (fig. S1). Seven membranes (M5 to M11) prepared using the 1-s plasma treatment yielded a sixfold higher H_2 permeance at 150°C, a slightly lower H_2/CH_4 selectivity (10.8 ± 2.0), and high H_2/C_3H_8 and H_2/SF_6 selectivities (45.8 ± 14.5 and 104 ± 4.2, respectively). The H_2 activation energy (19.0 ± 2.1 kJ mol^{-1}) was similar to that from the intrinsic defects, indicating that the majority of the pores formed during the plasma treatment consisted of similar electron density gap as those in the intrinsic defects. The slight loss in H_2/CH_4 selectivity can be attributed to the expansion of intrinsic defects upon plasma treatment. For the molecules with kinetic diameters smaller than 0.38 nm, the overall transport was in the activated regime where the activation energy increased with the molecular size (activation energies of He, H_2, CO_2, and CH_4 were 14.1 ± 0.5, 19.0 ± 2.1, 26.5 ± 0.5, and 26.3 ± 4.3 kJ mol^{-1}, respectively; Fig. 4C), indicating that the majority of the nanopores were smaller than 0.38 nm (*2*, *6*, *11*). The overall transport of the larger molecules (C_3H_8 and SF_6) had a substantial contribution from the gas-phase effusion, where in contrast to the activated transport, the flux decreases at a higher temperature (tables S1 to S3). Since the net flux is the sum of transport from pores yielding activated and effusive transport (Eq. 1), the percentage of pores yielding effusive transport can be extracted from the selectivity data (Eq. 2, note S3, and table S4).

$$\text{Permeance}_{\text{gas } i} = C_e N_{e,\text{gas } i} + C_a N_{a,\text{gas } i} \quad (1)$$

$$\alpha_{ij} = \left(\frac{N_{a,\text{gas } i}}{N_{a,\text{gas } j}}\right)\left(\frac{1 + \frac{C_e}{C_a}\frac{N_{e,\text{gas } i}}{N_{a,\text{gas } i}}}{1 + \frac{C_e}{C_a}\frac{N_{e,\text{gas } j}}{N_{a,\text{gas } j}}}\right) \quad (2)$$

Here, $N_{e,\text{gas } i}$ and $N_{a,\text{gas } i}$ are the permeation coefficients for the effusive and the activated transport, respectively. C_e and C_a correspond to

Downloaded from http://advances.sciencemag.org/ on January 27, 2019

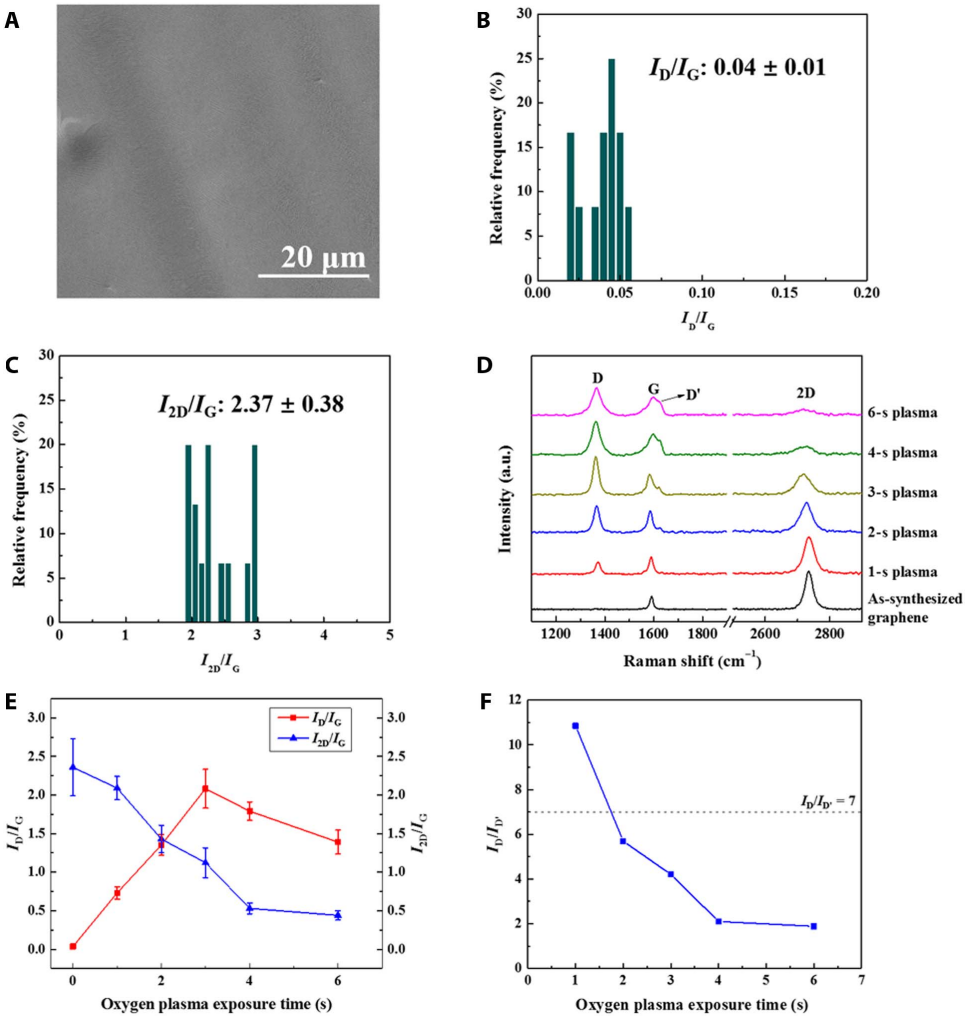

Fig. 2. Characterization of the as-synthesized and the plasma-treated graphene. (**A**) Scanning electron microscopy (SEM) image of the as-synthesized graphene on a Cu foil. Histograms of (**B**) I_D/I_G and (**C**) I_{2D}/I_G from the as-synthesized graphene. (**D**) Evolution of D, G, D′, and 2D peaks as a function of the plasma time (baseline subtracted from the Raman spectra). Corresponding evolution of (**E**) I_D/I_G, I_{2D}/I_G, and (**F**) $I_D/I_{D'}$ with respect to the plasma time. a.u., arbitrary units.

the density of pores contributing to the effusive and the activated transport, respectively. α_{ij} is the gas pair selectivity. On the basis of Eq. 2, the concentrations of pores larger than 0.38, 0.43, and 0.55 nm were only 35, 11, and 9 ppm, respectively (table S4).

Increasing the plasma exposure time to 2 s increased the nanopore density to 5.7×10^{11} cm^{-2} (fig. S1). As expected, the hydrogen permeance increased (membranes M12 and M13, 4041 ± 1323 GPU at 150°C; Fig. 4A). However, a small population of the preexisting pores was substantially expanded to above 0.43 nm, leading to poor H_2/CH_4 and H_2/C_3H_8 selectivities (Fig. 4B). The overall transport was still activated with activation energies comparable to that in the case of the 1-s plasma treatment (Fig. 4C), indicating that the majority of the pores were still small enough to operate in the size-sieving mode. The H_2/SF_6 selectivity was 17.7, much higher than the corresponding Knudsen selectivity of 8.5. On the basis of Eq. 2, the concentration of pores larger than 0.55 nm was 96 ppm (table S4).

Controlled pore expansion by O_3 treatment

The graphene treated with 1-s plasma comprised a substantial population of defects that did not contribute to H_2 permeation. An estimate of the defect density from the carbon amorphization trajectory (fig. S1 and note S4) indicates that the defect density in graphene increased by ca. 20-fold (1.5×10^{10} to 3.0×10^{11} cm^{-2}) after 1-s plasma exposure. However, the H_2 permeance only increased by ca. sixfold, indicating that majority of the defects introduced by 1-s plasma were either sp^3 defects (oxygen-functionalized sites) or vacancy defects with an electron density gap much smaller than 2.9 Å, making no contribution to the hydrogen transport. The sp^3 and the small vacancy defects can be considered as nuclei that can eventually grow into hydrogen-sieving nanopores. Since 2-s plasma led to an undesirable pore expansion for the H_2/CH_4 separation, a milder and more controllable pore expansion approach is needed such that the percentage of pores larger than 0.38 nm is limited to a few parts per million to achieve an attractive H_2/CH_4 selectivity. In this respect, the O_3-based lattice etching is a promising method (*25*, *26*). The atomic oxygen present in O_3 can effectively abstract the carbon in the graphene lattice, where the etching rate is expected to be proportional to temperature and the concentration of oxygen atoms, which, in turn, depends on O_3 concentration and temperature.

To convert the nuclei from the 1-s plasma treatment into the hydrogen-sieving pores, we exposed the plasma-treated graphene

Downloaded from http://advances.sciencemag.org/ on January 27, 2019

membranes to O_3 for a few seconds in the temperature range of 60° to 150°C. To accurately evaluate the effect of O_3 treatment on the nucleus expansion, the O_3 exposure was carried out in situ, in the permeation setup, right after measuring the molecular transport properties of the plasma-treated graphene. O_3 exposure to the plasma-treated graphene membrane (M9) at 60°C for 85 s almost doubled the H_2 permeance (from 672 to 1340 GPU at 150°C), while the CH_4 and the C_3H_8 permeances increased by a smaller amount (Fig. 5A and table S5). As a result, the H_2/CH_4 and the H_2/C_3H_8 selectivities increased to 16.1 from 11.0 and to 32.6 from 30.2, respectively. The method was reproducible. Another plasma-treated graphene (M7), upon the O_3 exposure, displayed similar results (fig. S3 and table S6).

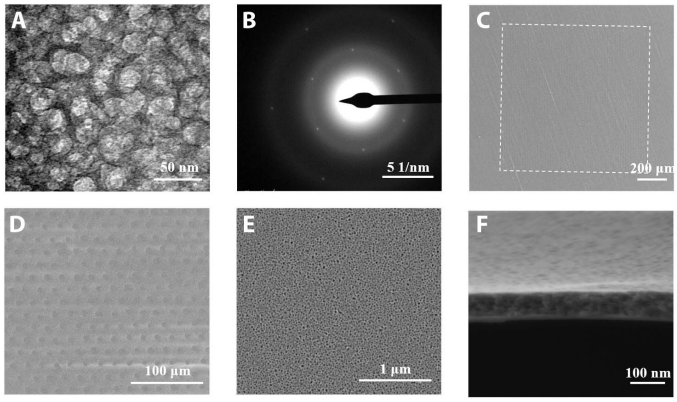

Fig. 3. Characterization of the NPC-supported graphene and the resulting membrane. (**A**) Transmission electron microscopy (TEM) image of the NPC/graphene revealing porous structure of NPC. (**B**) ED pattern of typical single-layer graphene observed throughout the sample. (**C** to **E**) SEM images of the NPC/graphene film on the macroporous W substrate with different magnifications. Graphene is sandwiched between the NPC film and the W substrate. The region surrounded by the white square in (C) represents a 1-mm^2 porous area on the W substrate. The circular features in (D) represent the arrays of 5-μm–sized macropores on the W substrate, visible in the SEM images because of electron beam–related charging effects. The porous structure of the NPC film is visible in (E). (**F**) Cross section of the NPC/graphene film revealing the thickness and the porous structure of the NPC film.

The O_3 exposure at a higher temperature was studied to understand the temperature-dependent activity of O_3. A much shorter exposure (10 s) at 150°C to the plasma-treated graphene (M10) resulted in an eightfold increase of H_2 permeance (698 to 6045 GPU) while also increasing the H_2/CH_4 selectivity (12.8 to 15.6; Fig. 5A and table S7). An extremely high H_2/SF_6 selectivity, 158, was achieved. The eightfold improvement in H_2 permeance and the synchronous enhancement in H_2/CH_4 selectivity by the high-temperature O_3 treatment suggest that the defect nucleation events were concurrent with the pore expansion, consequently increasing the population and the percentage of the hydrogen-sieving pores (table S8). To confirm this, we exposed an as-synthesized graphene membrane (M2) to O_3 at 150°C for 10 s. Here, the H_2 permeance increased by 15-fold (161 to 2581 GPU), while the H_2/CH_4 and H_2/C_3H_8 selectivities increased to 30 and 207, respectively (Fig. 5B and table S9), which verifies that the 150°C O_3 treatment leads to nucleation events as well. It seems that compared with the O_3 treatment at 60°C, the O_3 treatment at 150°C activates pore nucleation to a relatively higher extent, which can be attributed to the fact that the ac-

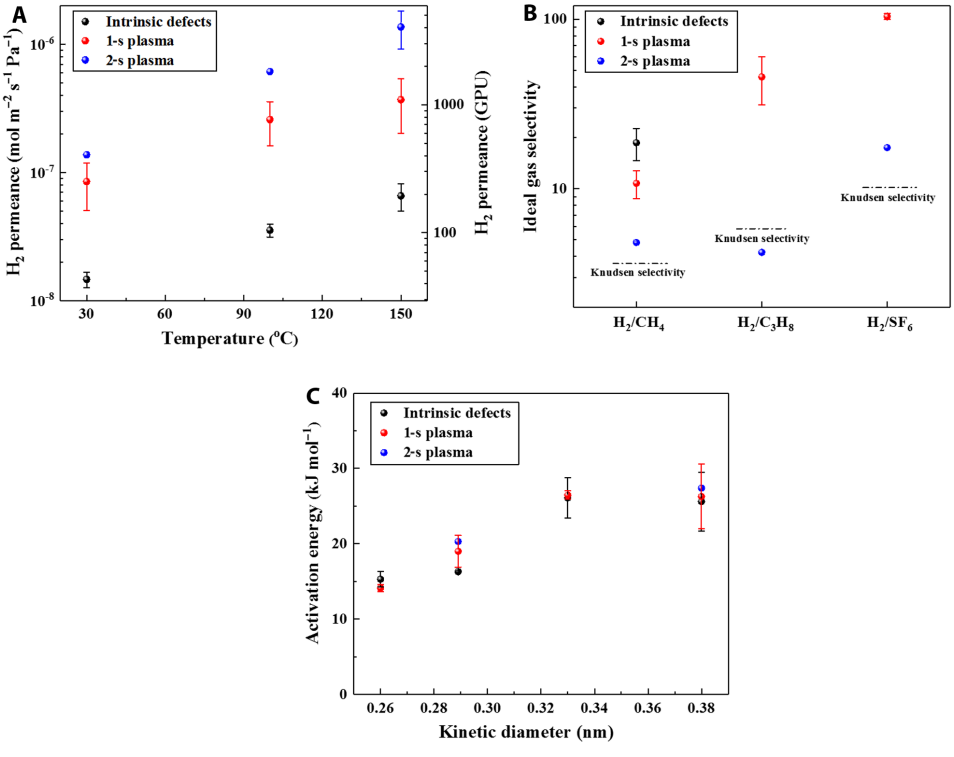

Fig. 4. Gas separation performance of graphene membranes from the intrinsic defects and from the pores generated by the plasma treatment. (**A**) Average H_2 permeance of graphene membranes as a function of temperature. The error bars correspond to SD across several membranes (four for intrinsic defects, seven for 1-s plasma, and two for 2-s plasma). (**B**) Corresponding ideal selectivities (ISs) at 150°C. The error bars correspond to SD across several membranes. (**C**) Activation energies for gases as a function of kinetic diameter and the plasma exposure time. The error bars correspond to SD across several membranes.

Downloaded from http://advances.sciencemag.org/ on January 27, 2019

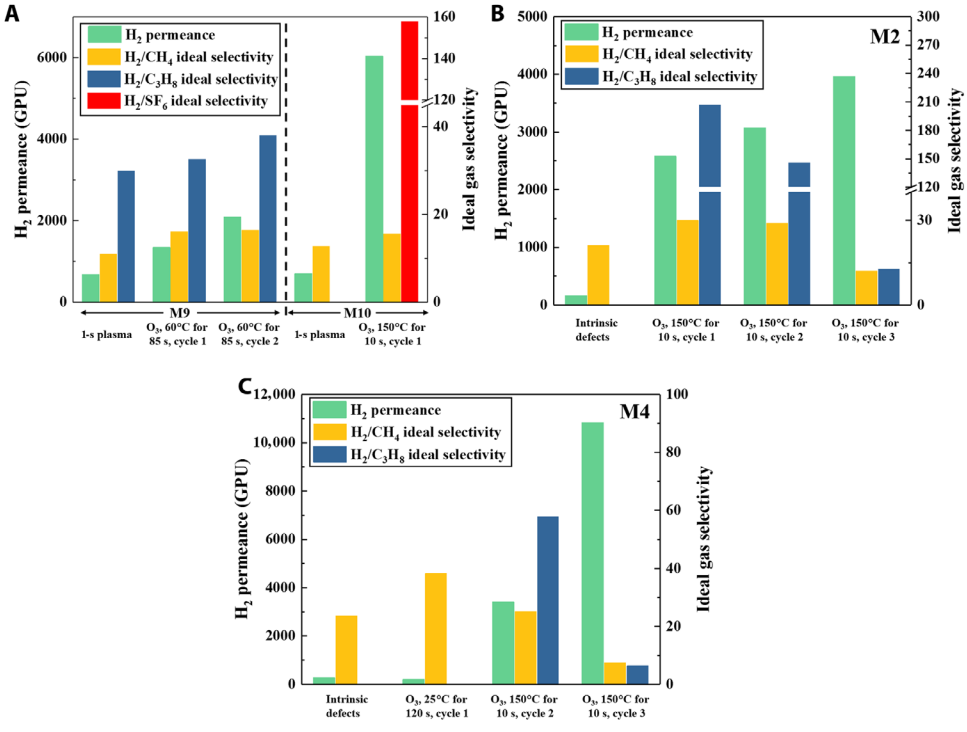

Fig. 5. Gas separation performance of graphene membranes before and after the O_3 treatment. (**A**) H_2 permeance and ideal gas selectivities of 1-s plasma-treated graphene M9 and M10 after O_3 treatment at 60°C (85 s) or 150°C (10 s). (**B**) H_2 permeance and ideal gas selectivities of M2 (intrinsic defects) after repeated O_3 treatments at 150°C (10 s). (**C**) H_2 permeance and ideal gas selectivities of M4 (intrinsic defects) after O_3 treatments at 25° C (120 s) and 150°C (10 s). The permeance and selectivity data were measured at 150°C.

tivation energy of carbon abstraction from the pristine graphene lattice is much higher than that from a defect site (*27*, *28*).

The pulsed O_3 treatment allowed us to further improve the H_2-sieving performance. For instance, the second cycle of O_3 treatment at 60°C for 85 s to membrane M9 substantially increased the H_2 permeance from 1340 to 2089 GPU while maintaining the H_2/CH_4 selectivity (16.1 to 16.5) and the H_2/C_3H_8 selectivity (32.6 to 38) (Fig. 5A and table S5). A similar trend was observed for the high-temperature O_3 treatment. The second cycle of treatment at 150 °C for 10 s to membrane M2 increased the H_2 permeance from 2581 to 3071 GPU while maintaining the H_2/CH_4 selectivity (30 to 29; Fig. 5B and table S9). A slight reduction of the H_2/C_3H_8 selectivity was observed (207 to 146), indicating expansion of the preexisting pores. The H_2 permeance was further improved by 30% using the third cycle of treatment; however, the H_2/CH_4 and the H_2/C_3H_8 selectivities decreased to 12.1 and 12.6, respectively.

Besides plasma treatment, we also investigated in situ room temperature O_3 treatment for incorporating sp^3 defects as nuclei in the graphene lattice. We recently demonstrated that the 25°C ozone functionalization incorporates ca. 6% sp^3 sites (epoxy and carbonyl groups) on the graphene lattice (*5*). In this experiment, the as-synthesized graphene, hosting only the intrinsic defects (M4), was exposed to O_3 at 25°C for 120 s. After this treatment, the H_2 permeance decreased from 268 to 194 GPU, and the H_2/CH_4 selectivity increased from 23.7 to 38.3 (Fig. 5C and table S10). This is caused by the oxygen functionalization of the pore edge, which shrinks the electron density gap in the nanopore. Subsequently, when the O_3 treatment (150°C for 10 s) was carried out to convert the sp^3 sites to nanopores, the H_2 permeance increased by 18-fold to 3400 GPU while maintaining an attractive H_2/CH_4 selectivity of 25.1 (Fig. 5C and table S10). The H_2/C_3H_8 selectivity was 57.8. In this case, repeating the treatment at 150°C led to the undesired pore expansion, reducing the H_2/CH_4 and the H_2/C_3H_8 selectivities to 7.5 and 6.4, respectively, albeit with a large H_2 permeance (10833 GPU).

Overall, the best H_2/CH_4 separation performance, which is a combination of high H_2 permeance and a moderate selectivity, was realized by the methods that maximize the density of size-sieving nanopores while restricting the percentage of nonselective effusive pores to less than 22 ppm (Fig. 6, A and B). The density of intrinsic defects, and defects generated by 1- and 2-s plasma, and "1 s plasma + 150°C O_3" was estimated using the I_D/I_G ratio employing the carbon amorphization trajectory. The pore density for the remaining samples was estimated by comparing the H_2 permeance. The advantages of the partially decoupled defect nucleation and pore expansion are evident, where the highest H_2 permeance is achieved (6045 GPU) with the corresponding H_2/CH_4 selectivities in the range of 15 to 25. Generally, the graphene etching methods lead to a trade-off between the pore density and the percentage of nonselective pores where the increase in the pore density often also leads to the increase in the density of nonselective pores. This is the case for the plasma treatment. The O_3 treatment works against this trade-off, where the pore density increased while the percentage of the nonselective pores decreased. This can be attributed to the following: (i) O_3 treatment increased the density of size-selective pores by up to two orders of magnitude, reducing the net percentage of nonselective pores, and (ii) O_3 treatment is expected to functionalize the pore edges, shrinking the electron density gap in the pores. This could, in principle, convert an effusive pore to a size-selective pore.

The separation performance of gas mixture is a crucial indicator of the membrane's efficacy in the industrial separation. The gas transport

Downloaded from http://advances.sciencemag.org/ on January 27, 2019

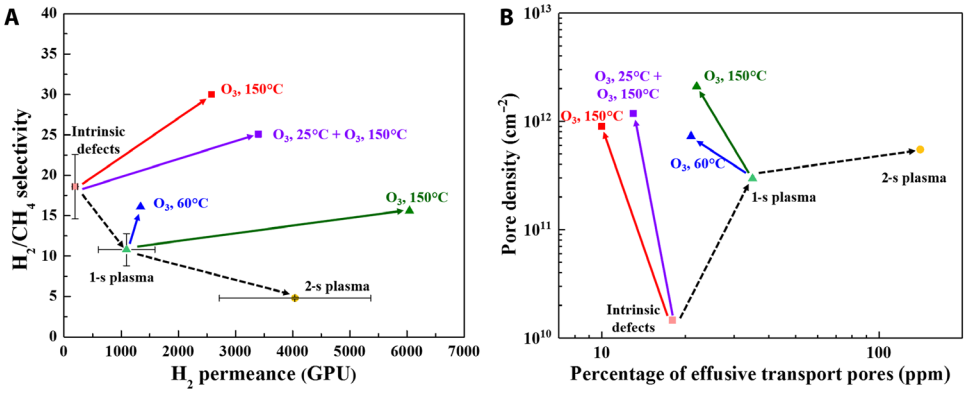

Fig. 6. Evolution of graphene nanopores and its impact on the separation performance. (**A**) H_2/CH_4 separation performance from the nanopores incorporated using the methods developed here. The data were obtained at 150°C. Data for the intrinsic defects and 1- and 2-s plasma were obtained by averaging the results of several membranes. The error bars correspond to the SD across several membranes (four for the intrinsic defects, seven for the 1-s plasma, and two for the 2-s plasma). (**B**) Evolution of the pore density and the percentage of pores larger than 0.38 nm.

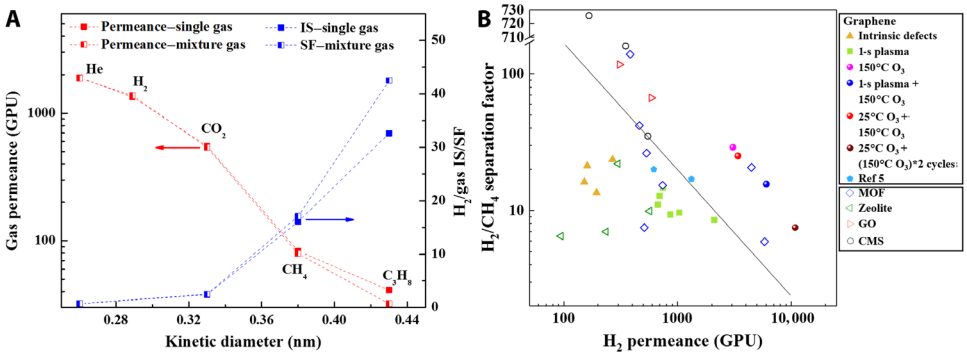

Fig. 7. Mixture separation performance of graphene membranes. (**A**) Comparison of graphene membrane performance in the single- and mixed-gas (equimolar) permeation tests (membrane M9 exposed to 60°C O_3 for 85 s). (**B**) Comparison of graphene membranes in this work with other membranes in the literatures in terms of the separation of H_2/CH_4 mixture (the gray line is the polymer upper bound assuming a 1-μm-thick selective layer). The performance of graphene membranes in this work is shown with the data from the single-gas permeation test, which is reasonable since the SF is equal or higher than the corresponding IS while the H_2 permeance does not change.

in several membrane materials (zeolites, MOFs, and polymers) is often determined by the competitive adsorption, and as a result, the mixture SFs can be lower than the corresponding single-component ideal selectivities (ISs). In the case of nanoporous graphene reported here, the adsorption energies are comparatively smaller than the activation energy for diffusion, and as a result, the gas transport is dominated by the activated diffusion. Consequently, the H_2 permeance was similar in the single-component and mixture cases (Fig. 7A). The mixture SFs were similar (H_2/He and H_2/CO_2) or slightly higher (H_2/CH_4 and H_2/C_3H_8) when compared with the corresponding single-component ISs.

The H_2/CH_4 separation performances reported here substantially exceed that from the 2008 Robeson upper bound for polymer membranes (assuming a 1-μm-thick selective layer) (*29*, *30*), with H_2 permeance surpassing that from the state-of-the-art membranes based on MOFs (*31*, *32*), zeolites (*33*, *34*), GO (*35*, *36*), and CMS (*37*, *38*) (Fig. 7B and table S11). In the context of H_2/CH_4 separation, such as recovery of hydrogen from the refinery off-gas streams (containing up to 35% hydrogen), a mixture SF of 20 is sufficient to obtain 90% recovery as well as 90% purity (*39*). Therefore, a high H_2 permeance with an SF of 20 can cut down the capital cost more substantially compared with the case of a low H_2 permeance with an SF close to 100.

DISCUSSION

In summary, we developed a partially decoupled pore nucleation and growth strategy using gaseous etchants that enabled etching time in the order of few seconds and yielded hydrogen-selective pores with a pore-size resolution of 1 Å. A high pore density, 2.1×10^{12} cm^{-2}, was realized where the concentration of pores larger than 0.38 nm was restricted to less than 22 ppm. As a result, the transport of the gas mixtures was controlled by the activation energy for pore translocation, and a record H_2/CH_4 mixture separation performance was achieved. Overall, the pore etching method discussed here works against the trade-off between the pore density and the PSD, is straightforward, scalable, and can be used to tune the pore size of graphene for separating a wide range of molecular mixtures. Moreover, the method can also be applied to generate the nanoporous lattice for several applications including sensing, catalysis, and energy storage and conversion.

MATERIALS AND METHODS

Materials and chemicals

The Cu foil (25 μm, 99.999% purity) was obtained from Alfa Aesar. Turanose (98.0%), *N*,*N*-dimethylformamide (99.8%), and $Na_2S_2O_8$ (99.0%) were purchased from Sigma-Aldrich. Poly(styrene-*b*-4-vinyl

Downloaded from http://advances.sciencemag.org/ on January 27, 2019

pyridine) [M_n(PS) = 11,800 g mol^{-1}, M_n(P4VP) = 12,300 g mol^{-1}, M_w/M_n = 1.08] was obtained from Polymer Source Inc. All chemicals were used as provided. All solutions were prepared with deionized (DI) water.

Membrane preparation

The single-layer graphene was synthesized using the LPCVD process on a Cu foil in a methane/hydrogen atmosphere. Before synthesis, the Cu foil was annealed at the growth temperature (1000°C) for 30 min in CO_2 and H_2 atmospheres, respectively. The as-synthesized CVD graphene, resting on the Cu foil, was exposed to radiofrequency-powered O_2 plasma (13.56 MHz, 17 W, 50 mtorr; EQ-PCE-3, MTI) to incorporate defects, with the exposure time ranging from 1 to 6 s. After that, the NPC-assisted transfer method was used to transfer graphene to the porous W support (*5*). Briefly, a solution of 0.1-g poly(styrene-*b*-4-vinyl pyridine) and 0.2-g turanose in 2 g of *N*,*N*-dimethylformamide was heated at 180°C for 3 hours and then spin coated (2000 rpm, 2 min) on the as-synthesized graphene. After drying at room temperature to allow phase separation, the polymer film was pyrolyzed at 500 °C for 1 hour in an Ar/H_2 atmosphere, forming the NPC film on the graphene surface. The NPC/graphene/Cu was pre-etched for 2 min with a 20 weight % $Na_2S_2O_8$ aqueous solution and then rinsed with water to remove the back-side graphene on the Cu foil. After a further 1 hour of etching, the Cu foil was completely etched, and the floating NPC/graphene was transferred to DI water for rinsing. Finally, a 50-μm-thick macroporous W substrate, comprising an array of 2900 laser-drilled 5-μm holes spread in a 1-mm^2 area, was used to scoop the NPC/graphene, forming the membrane. Before scooping, the W substrate was treated in the plasma for 2 min to increase the surface hydrophilicity, facilitating the transfer process. O_3 treatment was performed in situ in the membrane module. A mixture of O_3 and O_2 was introduced into the permeate side of the membrane module from an O_3 generator (Atlas 30, Absolute Ozone). The residence time of O_3 between the O_3 source and the membrane was 35 s (fig. S4 and note S5), and the O_3 concentration in the module sharply increased from 0 to 50 g/Nm^3 beyond 35 s. The O_3 treatment time reported here strictly corresponds to the time duration of O_3 exposure inside the membrane module and excludes the 35-s residence time between the generator and the membrane module.

Gas permeation test

The single-gas and mixture-gas permeation tests were performed in a homemade permeation cell (fig. S5). The W substrate acted both as a membrane support and a gasket in the membrane module (VCR, Swagelok) to achieve a leak-tight connection. Ar was used as the sweep gas. The flow rates of the feed and the sweep gas were controlled via mass flow controllers. The pressure on the feed side was maintained at 2 bar. Before each test, the membrane was heated to 150°C to desorb the adsorbed contaminants on the graphene surface (fig. S6, table S12, and note S6). The permeate gas concentration was analyzed in real time by a mass spectrometer (HPR-20, Hiden Analytical). The data were recorded and averaged after reaching the steady-state condition (typically 30 min after changing the operation conditions). The gas permeance *J*, IS α (for single-gas test), and SF β (for mixture-gas test) were calculated by the following equations

$$J_i = X_i/(A^*\Delta P_i) \quad (3)$$

$$\alpha_{ij} = J_i/J_j \quad (4)$$

$$\beta_{ij} = (C_i/C_j)_{\text{permeate}}/(C_i/C_j)_{\text{feed}} \quad (5)$$

where X_i is the flow rate of the component *i*, *A* is the membrane area, ΔP_i is the transmembrane pressure difference of component *i*, and C_i and C_j are the concentrations of component *i* and *j* in feed or permeate with *i* being the faster permeating component.

Graphene characterization

SEM was carried out to observe the morphology of graphene/Cu foil and NPC/graphene as well as the thickness of the NPC film. An FEI Teneo scanning electron microscope with an operating voltage of 0.8 to 2.0 kV and a working distance of 2.5 to 7.0 mm was used. The samples were directly characterized without any conductive coating. Transmission electron microscopy (TEM) imaging of the NPC film and ED of the NPC/graphene film were conducted using an FEI Tecnai G2 Spirit microscope operating with a 120-keV incident electron beam.

Raman characterization was performed on graphene/Cu using a Renishaw micro-Raman spectroscope (457 nm, 2.33 eV, 50× objective). More than 10 spectra were collected with the mapping method for each sample. The Raman data were analyzed by curve fitting in MATLAB to extract the I_D/I_G, $I_D/I_{D'}$, and I_{2D}/I_G ratios. Before analysis, the background was subtracted from the Raman spectra.

SUPPLEMENTARY MATERIALS

Supplementary material for this article is available at http://advances.sciencemag.org/cgi/content/full/5/1/eaav1851/DC1

Note S1. High-resolution TEM (HRTEM)–based characterization of graphene.
Note S2. Calculation of activation energy.
Note S3. Estimation of the percentage of the nonselective nanopores in graphene.
Note S4. Estimation of the defect density from Raman.
Note S5. Measurement of the O_3 residence time.
Note S6. Desorption of contaminants before permeation test.
Fig. S1. The correlation between L_d, n_d, and I_D/I_G.
Fig. S2. HRTEM image of graphene after 6-s plasma treatment.
Fig. S3. Gas permeation performance of 1-s plasma-treated graphene M7 after 60°C O_3 treatment for 85 s.
Fig. S4. The rise of O_3 concentration in membrane module.
Fig. S5. Schematic of the setup for gas permeation test.
Fig. S6. Gas permeation performance of 1-s plasma-treated graphene M14.
Table S1. Gas permeance from M1 to M13 at 150°C.
Table S2. Gas permeance from M1 to M13 at 100°C.
Table S3. Gas permeance from M1 to M13 at 30°C.
Table S4. Estimated percentage of large nanopores in graphene after O_2 plasma exposure for different gas molecules.
Table S5. Gas permeance from M9 before and after O_3 etching at 60°C for 85 s.
Table S6. Gas permeance from M7 before and after O_3 etching at 60°C for 85 s.
Table S7. Gas permeance from M10 before and after O_3 etching at 150°C for 10 s.
Table S8. Percentage of nanopores larger than 0.38 nm after post cycles of O_3 etching.
Table S9. Gas permeance from M2 before and after O_3 etching at 150°C for 10 s.
Table S10. Gas permeance from M4 before and after O_3 etching.
Table S11. Comparison of H_2/CH_4 separation performance in this work with that in other literatures.
Table S12. Gas permeance from M14 (1-s plasma-treated membrane) before and after 150°C treatment used to remove contaminants.
References (*40*–*51*)

REFERENCES AND NOTES

1. S. P. Koenig, L. Wang, J. Pellegrino, J. S. Bunch, Selective molecular sieving through porous graphene. *Nat. Nanotechnol.* **7**, 728–732 (2012).

Downloaded from http://advances.sciencemag.org/ on January 27, 2019

2. K. Celebi, J. Buchheim, R. M. Wyss, A. Droudian, P. Gasser, I. Shorubalko, J.-I. Kye, C. Lee, H. G. Park, Ultimate permeation across atomically thin porous graphene. *Science* **344**, 289–292 (2014).
3. L. Wang, L. W. Drahushuk, L. Cantley, S. P. Koenig, X. Liu, J. Pellegrino, M. S. Strano, J. S. Bunch, Molecular valves for controlling gas phase transport made from discrete ångström-sized pores in graphene. *Nat. Nanotechnol.* **10**, 785–790 (2015).
4. S. P. Surwade, S. N. Smirnov, I. V. Vlassiouk, R. R. Unocic, G. M. Veith, S. Dai, S. M. Mahurin, Water desalination using nanoporous single-layer graphene. *Nat. Nanotechnol.* **10**, 459–464 (2015).
5. S. Huang, M. Dakhchoune, W. Luo, E. Oveisi, G. He, M. Rezaei, J. Zhao, D. T. L. Alexander, A. Züttel, M. S. Strano, K. V. Agrawal, Single-layer graphene membranes by crack-free transfer for gas mixture separation. *Nat. Commun.* **9**, 2632 (2018).
6. L. Wang, M. S. H. Boutilier, P. R. Kidambi, D. Jang, N. G. Hadjiconstantinou, R. Karnik, Fundamental transport mechanisms, fabrication and potential applications of nanoporous atomically thin membranes. *Nat. Nanotechnol.* **12**, 509–522 (2017).
7. D.-e. Jiang, V. R. Cooper, S. Dai, Porous graphene as the ultimate membrane for gas separation. *Nano Lett.* **9**, 4019–4024 (2009).
8. H. Du, J. Li, J. Zhang, G. Su, X. Li, Y. Zhao, Separation of hydrogen and nitrogen gases with porous graphene membrane. *J. Phys. Chem. C* **115**, 23261–23266 (2011).
9. L. W. Drahushuk, M. S. Strano, Mechanisms of gas permeation through single layer graphene membranes. *Langmuir* **28**, 16671–16678 (2012).
10. H. Liu, S. Dai, D.-e. Jiang, Insights into CO_2/N_2 separation through nanoporous graphene from molecular dynamics. *Nanoscale* **5**, 9984–9987 (2013).
11. Z. Yuan, A. G. Rajan, R. P. Misra, L. W. Drahushuk, K. V. Agrawal, M. S. Strano, D. Blankschtein, Mechanism and prediction of gas permeation through sub-nanometer graphene pores: Comparison of theory and simulation. *ACS Nano* **11**, 7974–7987 (2017).
12. C. Moreno, M. Vilas-Varela, B. Kretz, A. Garcia-Lekue, M. V. Costache, M. Paradinas, M. Panighel, G. Ceballos, S. O. Valenzuela, D. Peña, A. Mugarza, Bottom-up synthesis of multifunctional nanoporous graphene. *Science* **360**, 199–203 (2018).
13. P. R. Kidambi, D. Jang, J.-C. Idrobo, M. S. H. Boutilier, L. Wang, J. Kong, R. Karnik, Nanoporous atomically thin graphene membranes for desalting and dialysis applications. *Adv. Mater.* **29**, 1700277 (2017).
14. K. V. Agrawal, J. D. Benck, Z. Yuan, R. P. Misra, A. G. Rajan, Y. Eatmon, S. Kale, X. S. Chu, D. O. Li, C. Gong, J. Warner, Q. H. Wang, D. Blankschtein, M. S. Strano, Fabrication, pressure testing, and nanopore formation of single-layer graphene membranes. *J. Phys. Chem. C.* **121**, 14312–14321 (2017).
15. S. Garaj, W. Hubbard, A. Reina, J. Kong, D. Branton, J. A. Golovchenko, Graphene as a subnanometre trans-electrode membrane. *Nature.* **467**, 190–193 (2010).
16. T. Gilboa, A. Zrehen, A. Girsault, A. Meller, Optically-monitored nanopore fabrication using a focused laser beam. *Sci. Rep.* **8**, 9765 (2018).
17. Y. Yamada, K. Murota, R. Fujita, J. Kim, A. Watanabe, M. Nakamura, S. Sato, K. Hata, P. Ercius, J. Ciston, C. Y. Song, K. Kim, W. Regan, W. Gannett, A. Zettl, Subnanometer vacancy defects introduced on graphene by oxygen gas. *J. Am. Chem. Soc.* **136**, 2232–2235 (2014).
18. A. Kaplan, Z. Yuan, J. D. Benck, A. G. Rajan, X. S. Chu, Q. H. Wang, M. S. Strano, Current and future directions in electron transfer chemistry of graphene. *Chem. Soc. Rev.* **46**, 4530–4571 (2017).
19. Y. Yin, A. P. Alivisatos, Colloidal nanocrystal synthesis and the organic–inorganic interface. *Nature.* **437**, 664–670 (2005).
20. R. Rozada, P. Solís-Fernández, J. I. Paredes, A. Martínez-Alonso, H. Ago, J. M. D. Tascón, Controlled generation of atomic vacancies in chemical vapor deposited graphene by microwave oxygen plasma. *Carbon.* **79**, 664–669 (2014).
21. X. Li, W. Cai, J. An, S. Kim, J. Nah, D. Yang, R. Piner, A. Velamakanni, I. Jung, E. Tutuc, S. K. Banerjee, L. Colombo, R. S. Ruoff, Large-area synthesis of high-quality and uniform graphene films on copper foils. *Science* **324**, 1312–1314 (2009).
22. A. C. Ferrari, D. M. Basko, Raman spectroscopy as a versatile tool for studying the properties of graphene. *Nat. Nanotechnol.* **8**, 235–246 (2013).
23. L. G. Cançado, A. Jorio, E. H. Martins Ferreira, F. Stavale, C. A. Achete, R. B. Capaz, M. V. O. Moutinho, A. Lombardo, T. S. Kulmala, A. C. Ferrari, Quantifying defects in graphene via raman spectroscopy at different excitation energies. *Nano Lett.* **11**, 3190–3196 (2011).
24. A. Eckmann, A. Felten, A. Mishchenko, L. Britnell, R. Krupke, K. S. Novoselov, C. Casiraghi, Probing the nature of defects in graphene by raman spectroscopy. *Nano Lett.* **12**, 3925–3930 (2012).
25. D.-P. Yang, X. Wang, X. Guo, X. Zhi, K. Wang, C. Li, G. Huang, G. Shen, Y. Mei, D. Cui, UV/O_3 generated graphene nanomesh: Formation mechanism, properties, and FET studies. *J. Phys. Chem. C.* **118**, 725–731 (2014).
26. H. Tao, J. Moser, F. Alzina, Q. Wang, C. M. Sotomayor-Torres, The morphology of graphene sheets treated in an ozone generator. *J. Phys. Chem. C.* **115**, 18257–18260 (2011).
27. X. Chu, L. D. Schmidt, Reactions of NO, O_2, H_2O, and CO_2 with the basal plane of graphite. *Surf. Sci.* **268**, 325–332 (1992).
28. R.-Z. Duant, R. T. Yang, Kinetics of the reaction between steam and the basal plane of graphite. *Chem. Eng. Sci.* **39**, 795–798 (1984).
29. H. B. Park, J. Kamcev, L. M. Robeson, M. Elimelech, B. D. Freeman, Maximizing the right stuff: The trade-off between membrane permeability and selectivity. *Science* **356**, eaab0530 (2017).
30. L. M. Robeson, The upper bound revisited. *J. Membr. Sci.* **320**, 390–400 (2008).
31. Z. Kang, M. Xue, L. Fan, L. Huang, L. Guo, G. Wei, B. Chen, S. Qiu, Highly selective sieving of small gas molecules by using an ultra-microporous metal–organic framework membrane. *Energy Environ. Sci.* **7**, 4053–4060 (2014).
32. F. Zhang, X. Zou, X. Gao, S. Fan, F. Sun, H. Ren, G. Zhu, Hydrogen selective NH_2-MIL-53(Al) MOF membranes with high permeability. *Adv. Funct. Mater.* **22**, 3583–3590 (2012).
33. H. Kalipcilar, T. C. Bowen, R. D. Noble, J. L. Falconer, Synthesis and separation performance of SSZ-13 zeolite membranes on tubular supports. *Chem. Mater.* **14**, 3458–3464 (2002).
34. C. Zhou, C. Yuan, Y. Zhu, J. Caro, A. Huang, Facile synthesis of zeolite FAU molecular sieve membranes on bio-adhesive polydopamine modified Al_2O_3 tubes. *J. Membr. Sci.* **494**, 174–181 (2015).
35. J. Yang, D. Gong, G. Li, G. Zeng, Q. Wang, Y. Zhang, G. Liu, P. Wu, E. Vovk, Z. Peng, X. Zhou, Y. Yang, Z. Liu, Y. Sun, Self-assembly of thiourea-crosslinked graphene oxide framework membranes toward separation of small molecules. *Adv. Mater.* **30**, 1705775 (2018).
36. H. Li, Z. Song, X. Zhang, Y. Huang, S. Li, Y. Mao, H. J. Ploehn, Y. Bao, M. Yu, Ultrathin, molecular-sieving graphene oxide membranes for selective hydrogen separation. *Science* **342**, 95–98 (2013).
37. H.-H. Tseng, C.-T. Wang, G.-L. Zhuang, P. Uchytil, J. Reznickova, K. Setnickova, Enhanced H_2/CH_4 and H_2/CO_2 separation by carbon molecular sieve membrane coated on titania modified alumina support: Effects of TiO_2 intermediate layer preparation variables on interfacial adhesion. *J. Membr. Sci.* **510**, 391–404 (2016).
38. C. Zhang, W. J. Koros, Ultraselective carbon molecular sieve membranes with tailored synergistic sorption selective properties. *Adv. Mater.* **29**, 1701631 (2017).
39. M. Pera-Titus, Porous inorganic membranes for CO_2 capture: Present and prospects. *Chem. Rev.* **114**, 1413–1492 (2014).
40. J. Schrier, Fluorinated and nanoporous graphene materials as sorbents for gas separations. *ACS Appl. Mater. Interfaces.* **3**, 4451–4458 (2011).
41. M. W. Cole, D. R. Frankl, D. L. Goodstein, Probing the helium-graphite interaction. *Rev. Mod. Phys.* **53**, 199–210 (1981).
42. R. Hellemans, A. Van Itterbeek, W. Van Dael, The adsorption of helium, argon and nitrogen on graphite. *Physica.* **34**, 429–437 (1967).
43. B. Wang, N. Hu, H. Wang, Y. Zheng, R. Zhou, Improved AlPO-18 membranes for light gas separation. *J. Mater. Chem. A.* **3**, 12205–12212 (2015).
44. A. Farjoo, S. M. Kuznicki, M. Sadrzadeh, Hydrogen separation by natural zeolite composite membranes: Single and multicomponent gas transport. *Materials* **10**, 1159 (2017).
45. A. Huang, Q. Liu, N. Wang, Y. Zhu, J. Caro, Bicontinuous zeolitic imidazolate framework ZIF-8@GO membrane with enhanced hydrogen selectivity. *J. Am. Chem. Soc.* **136**, 14686–14689 (2014).
46. A. Huang, W. Dou, J. Caro, Steam-stable zeolitic imidazolate framework ZIF-90 membrane with hydrogen selectivity through covalent functionalization. *J. Am. Chem. Soc.* **132**, 15562–15564 (2010).
47. H. Guo, G. Zhu, I. J. Hewitt, S. Qiu, "Twin copper source" growth of metal–organic framework membrane: $Cu_3(BTC)_2$ with high permeability and selectivity for recycling H_2. *J. Am. Chem. Soc.* **131**, 1646–1647 (2009).
48. F. Hillman, J. Brito, H.-K. Jeong, Rapid one-pot microwave synthesis of mixed-linker hybrid zeolitic-imidazolate framework membranes for tunable gas separations. *ACS Appl. Mater. Interfaces.* **10**, 5586–5593 (2018).
49. P. Nian, Y. Li, X. Zhang, Y. Cao, H. Liu, X. Zhang, ZnO nanorod-induced heteroepitaxial growth of SOD type Co-based zeolitic imidazolate framework membranes for H_2 separation. *ACS Appl. Mater. Interfaces.* **10**, 4151–4160 (2018).
50. H.-C. Lee, M. Monji, D. Parsley, M. Sahimi, P. Liu, F. Egolfopoulos, T. Tsotsis, Use of steam activation as a post-treatment technique in the preparation of carbon molecular sieve membranes. *Ind. Eng. Chem. Res.* **52**, 1122–1132 (2013).
51. A. K. Itta, H.-H. Tseng, M.-Y. Wey, Fabrication and characterization of PPO/PVP blend carbon molecular sieve membranes for H_2/N_2 and H_2/CH_4 separation. *J. Membr. Sci.* **372**, 387–395 (2011).

Acknowledgments: We are grateful to E. Oveisi for help with the HRTEM imaging. **Funding:** This work was supported by the host institution (EPFL), the ETH board, the Swiss National Science Foundation (Assistant Professor Energy Grant; grant number PYAPP2_173645), and the Swiss Competence Center for Energy Research–Efficiency of Industrial Processes (SCCER-EIP, Phase II; grant number 1155002538). **Author contributions:** K.V.A. and J.Z. conceived the project. J.Z. and G.H. designed, fabricated, and tested the

Downloaded from http://advances.sciencemag.org/ on January 27, 2019

graphene membranes. J.Z. performed Raman characterization. S.H. developed the graphene synthesis procedure. L.F.V. performed TEM characterization. M.D. and S.H. developed the NPC film. M.D. and J.Z. performed SEM characterization. H.B. developed the MATLAB analysis of Raman data. K.V.A., S.H., G.H., and J.Z. built the CVD and the membrane setup. J.Z., G.H., and K.V.A. wrote the paper. All authors revised the paper. **Competing interests:** The authors declare they have no competing interests. **Data and materials availability:** All data needed to evaluate the conclusions in the paper are present in the paper and/or the Supplementary Materials. Additional data related to this paper may be requested from the authors.

Submitted 23 August 2018
Accepted 10 December 2018
Published 25 January 2019
10.1126/sciadv.aav1851

Citation: J. Zhao, G. He, S. Huang, L. F. Villalobos, M. Dakhchoune, H. Bassas, K. V. Agrawal, Etching gas-sieving nanopores in single-layer graphene with an angstrom precision for high-performance gas mixture separation. *Sci. Adv.* **5**, eaav1851 (2019).

Downloaded from http://advances.sciencemag.org/ on January 27, 2019

Science Advances

Etching gas-sieving nanopores in single-layer graphene with an angstrom precision for high-performance gas mixture separation

J. Zhao, G. He, S. Huang, L. F. Villalobos, M. Dakhchoune, H. Bassas and K. V. Agrawal

Sci Adv **5** (1), eaav1851.
DOI: 10.1126/sciadv.aav1851

ARTICLE TOOLS http://advances.sciencemag.org/content/5/1/eaav1851

SUPPLEMENTARY MATERIALS http://advances.sciencemag.org/content/suppl/2019/01/18/5.1.eaav1851.DC1

REFERENCES This article cites 51 articles, 5 of which you can access for free
http://advances.sciencemag.org/content/5/1/eaav1851#BIBL

PERMISSIONS http://www.sciencemag.org/help/reprints-and-permissions

Use of this article is subject to the Terms of Service

Science Advances (ISSN 2375-2548) is published by the American Association for the Advancement of Science, 1200 New York Avenue NW, Washington, DC 20005. 2017 © The Authors, some rights reserved; exclusive licensee American Association for the Advancement of Science. No claim to original U.S. Government Works. The title *Science Advances* is a registered trademark of AAAS.

Downloaded from http://advances.sciencemag.org/ on January 27, 2019